Explaining Kinetic Trends of Inner-sphere Transition Metal Ion Redox Reactions at Electrodes for Vanadium Redox Flow Batteries

Introduction and Background

A better understanding of the kinetics of heterogeneous inner-sphere metal-ion charge transfer (CT) reactions is relevant for electroplating, chemical sensors, corrosion prevention, and energy storage. For example, vanadium redox flow batteries (VRFBs) are a promising grid-scale energy storage technology that could help enable the transition to a clean energy grid reliant on intermittent renewables like solar and wind, reducing our dependence on fossil fuels.[1]
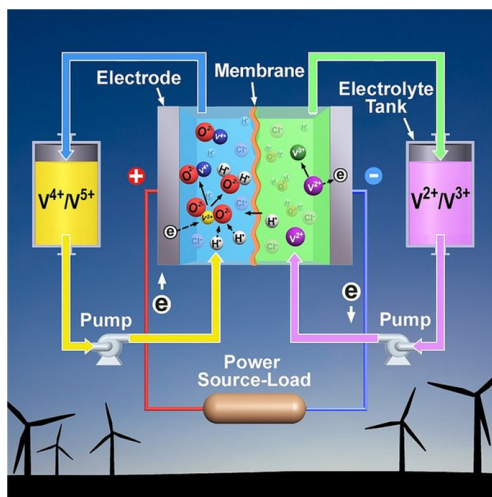

Figure 1. Schematic of a vanadium redox flow battery (VRFB) during a discharging cycle. During a charging cycle, the electrons would move in the opposite direction and the load would become a power source. The two half-cells are separated by an ion-exchange membrane, which allows H$^+$ ions, but not vanadium ions, to move from one half-cell to the other. Pumps are used to transport the redox-active ions between the electrolyte tanks and the cell containing the electrode. Figure taken from ref. 1.

VFRBs store vanadium ions of different oxidation states in large tanks and use a redox reaction to charge and discharge the battery by flowing the metal ions across an electrode. One tank stores the anolyte (V^{2+}/V^{3+}) while the other stores the catholyte (VO_2^+/VO^{2+}). When the battery is fully charged, the anolyte contains only V^{2+} and the catholyte only VO_2^+ (in which vanadium is in the +5 oxidation state). When the battery is fully discharged, the anolyte contains only V^{3+} and the catholyte only VO^{2+} (in which vanadium is in the 4+ oxidation state). The state of charge (SoC) is defined as follows:[2]

$$SoC = \frac{[V^{2+}]}{[V^{2+}]+[V^{3+}]} \qquad (1)$$

Where $[V^{2+}]$ and $[V^{3+}]$ are the concentrations of vanadium in the 2+ and 3+ oxidation states, respectively, in the anolyte. When solar and wind energy are available (for example during the day) and electricity supply exceeds demand, the flow battery is charged by oxidizing VO^{2+} to VO_2^+ and reducing V^{3+} to V^{2+} rather than letting the excess electricity go to waste. When solar and wind energy are not available (for example after the sun sets) and electricity demand exceeds supply, rather than using fossil fuels to meet demand, the battery can be discharged by oxidizing V^{2+} to V^{3+} and reducing VO_2^+ to VO^{2+}. VFRBs have

received considerable investment in recent years due to their decoupled power output and storage capacity, long lifetimes, and lack of cross-contamination due to the use of vanadium ions in both half-cells. However, the sluggish kinetics of the V^{2+}/V^{3+} redox couple results in large overpotentials, limiting round-trip energy efficiency and requiring the use of electrodes with large surface areas to achieve the desired current. Previous work using extended X-ray absorption fine structure (EXAFS) spectroscopy has identified the structure of V^{2+}/V^{3+} in perchloric acid as a hexa-aqua complex with six water molecules in the coordination sphere and with a chloride or sulfate ion substituted for one of the water molecules in hydrochloric and sulfuric acid, respectively.[2] In addition, the anion entering the coordination sphere is able to act as a bridging ligand that enables the vanadium ion to adsorb and transfer an electron to the electrode surface, and the energy of the adsorbed intermediate relative to the desorbed state determines CT kinetics.[2,3] CT involving the formation of a chemical bond between the electrode and redox-active species is termed inner-sphere, as opposed to outer-sphere CT which occurs between two separate species with no bond formation. Heterogeneous CT occurs at the interface between two different phases (e.g. liquid/solid or gas/solid); therefore this reaction is termed a heterogeneous inner-sphere metal-ion charge transfer (het-CT) reaction. Because inner-sphere CT occurs more rapidly than outer-sphere CT, this explains why the presence of halide ions (i.e. Cl^-, Br^-, and I^- in the form of hydrochloric, hydrobromic, or hydroiodic acid, respectively), which form a bridge between the vanadium complex and the electrode, enhance the V^{2+}/V^{3+} CT kinetics.[4] Previous work found that CT kinetics on glassy carbon increase going from Cl to Br to I due to an increase in the energy of the adsorbed intermediate.[3] This can be explained by the Sabatier principle, which states that there exists an optimal adsorption strength that maximizes the rate of a catalytic reaction.[5,6] Furthermore, halide-induced rate enhancement is also observed for a variety of other het-CT reactions relevant to energy storage, including Zn/Zn^{2+}, Cr^{2+}/Cr^{3+} and Fe^{2+}/Fe^{3+} on both glassy carbon and metal electrodes, indicating that this effect is general for metal-ion charge transfer.[4] In addition to changing the electrolyte, the adsorption strength can also be tuned by changing the electrode identity, and the large number of metals in the periodic table allow for a wide range of possibilities. Although we hypothesize the same anion bridging mechanism holds for het-CT on metal electrodes, this has not been proven experimentally, nor has the effect of the electrode on het-CT kinetics been well-studied. A better understanding of the effect of metal electrode identity on het-CT kinetics could enable the design of more effective electrocatalysts for redox flow battery applications.

The *d*-band model, which describes bonding at a transition metal surface in terms of the interactions between the valence electrons of an adsorbate and the *d* electrons (or *d*-states) of the metal and the filling of antibonding orbitals,[7] uses the *d*-band center (or average energy of the *d*-states of a transition metal relative to the Fermi level, or the energy level of the highest state occupied by electrons) as a descriptor for the adsorption energy of *p*-block adorbates on transition metal surfaces, and therefore the kinetics of heterogeneous catalytic reactions based on Brønsted−Evans−Polanyi (BEP) relations.[5] This project aims to extend the *d*-band model to het-CT reactions, which involve the adsorption and charge transfer of metal ions at transition metal electrodes. Our hypothesis is that variations in het-CT kinetics across different transition metal electrodes are due to variations in the energy of the adsorbed intermediate, which are determined by the *d*-band center of the electrode. Using kinetic measurements, microkinetic modeling, and density functional theory (DFT)-calculated adsorption energies, we show that adsorption energy of the adsorbed surface intermediate for the V^{2+}/V^{3+} CT reaction indeed correlates strongly with electrode *d*-band center for eight different transition metals. We also show that the adsorption energy of the

vanadium intermediate relates to exchange current density for five experimentally tested metals, with tungsten (W) having the highest d-band center, strongest adsorption energy, and most active kinetics. We also show that the electrode d-band center correlates with experimentally determined apparent rate constants and exchange current densities for a variety of het-CT reactions from the literature.

Methods

I evaluated the adsorption free energy of the proposed *[O─V(H_2O)_4SO_4] intermediate on metal surfaces using DFT-based metadynamics simulations ran in the Vienna *ab-initio* Simulation Package (VASP). Metadynamics is a method of biased molecular simulation that uses artificial bias potentials to fill gaps in the free energy surface expressed in terms of a collective variable that describes the large-scale motions of the system.[8,9] I used the z-coordinate of the vanadium ion, which is indicative of the distance between the vanadium-ion complex and the metal surface, as the collective variable.[4] Once the free energy minimum associated with the adsorbed state is filled, the complex desorbs and the free energy of adsorption is estimated from the depth of the potential well built up from the sum of the bias potentials (or "Gaussian hills").

I modeled the surfaces of Au, Ag, Cu, Bi, W, Ta, Cr, Fe, and Rh using the most stable crystal structures and surface facets of each metal (e.g. fcc(111) or bcc(110)). The projector augmented wave (PAW) method was used to describe electron-ion interactions.[10] The Perdew-Burke-Ernzerhof (PBE) exchange-correlation functional was used for all calculations with a plane wave energy cutoff of 400 eV.[11] Spin-polarized DFT was used with a spin density of two spin-up electrons to model the V^{3+} ion. A three-layer thick 4×4 slab was used as the simulation cell with the middle layer fixed. A gamma-centered k-point mesh was used to sample the Brillouin zone. The cell was initialized with *[HO─V(H_2O)_4SO_4] and 42 explicit water molecules with a bulk density of 1 g/cm^3. However, during equilibration, the hydrogen ion dissociated into the surrounding media and a *[O─V(H_2O)_4SO_4] intermediate was formed. An image of this simulation cell is shown in **Figure 2** below for Au(111).

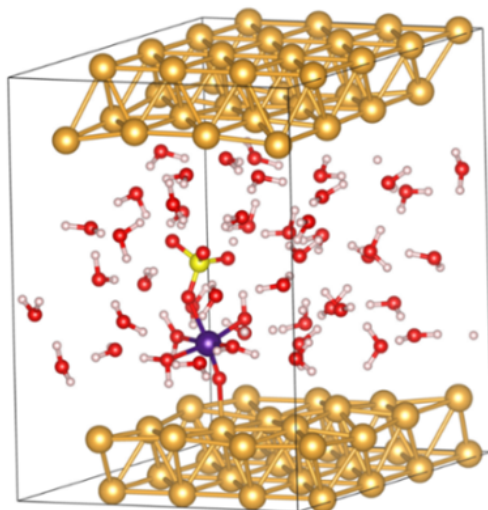**Figure 2.** Simulation cell used to evaluate the adsorption energy of *[O─V(H$_2$O)$_4$SO$_4$] on Au(111) using metadynamics. The simulation cell size is 11.8 × 11.8 × 18.0 Å. Atom color legend: red = O, yellow = Au, light yellow = S, purple = V, and white = H.

In order to equilibrate the system at the desired temperature of 300 K prior to running metadynamics, a Nosé-Hoover thermostat was used for at least 5 ps with a time step of 0.5 fs.[12]

Once the system was equilibrated, metadynamics was initialized. Gaussian bias potentials with height 0.01 eV and width 0.10 Å were deposited every 15 fs. The width of the Gaussian hills was based on the standard deviation of changes in the collective variable during equilibration. Once the adsorption energy stopped increasing and a second free energy minimum started to form in the desorbed state, the complex was desorbed from the surface and metadynamics terminated.

Gas-phase adsorption free energies of *[HO─V(H$_2$O)$_4$SO$_4$] are calculated using static gas-phase DFT calculations and using equation (2) below, where ΔG_{ads} is the gas-phase adsorption free energy, $G_{slab+V-ion\ complex}$ is the free energy of the vanadium-ion complex adsorbed on the most stable facet of each metal considered, $G_{V-ion\ complex}$ is the free energy of the isolated [HO─V(H$_2$O)$_4$SO$_4$] species, and G_{slab} is the electronic energy of the bare slab in vacuum:

$$\Delta G_{ads} = G_{slab+V-ion\ complex} - G_{V-ion\ complex} - G_{slab} \tag{2}$$

Free energies are calculated using the harmonic oscillator model as implemented in the Atomic Simulation Environment (ASE),[13] in which all degrees of freedom are treated as harmonic vibrations. We consider zero-point vibrational energies, vibrational heat capacities, and entropic effects in the free energy calculations. We neglect vibrational free energy contributions from the metal slab and effects due to changes in volume. Free energies are calculated using equation (3), where G is the free energy, E_{elec} is the electronic DFT energy, E_{ZPE} is the zero-point energy, ε_i are the vibrational energies, k_B is Boltzmann's constant, T is the absolute temperature (300 K), and S is the entropy. The summation is over the vibrational energies of all degrees of freedom of the molecule, calculated using DFT:

$$G = E_{elec} + E_{ZPE} + \sum_{harm\ DOF}\left[\frac{\epsilon_i}{exp\left(\epsilon_i/k_BT\right)-1}\right] - TS \tag{3}$$

The entropy is given by equation 4:

$$S = k_B \sum_{harm\ DOF}\left[\frac{\epsilon_i}{k_BT(exp\left(\epsilon_i/k_BT\right)-1)} - ln(1 - exp(\frac{-\epsilon_i}{k_BT}))\right] \tag{4}$$

Unless stated otherwise, the same DFT settings used for metadynamics were used for the gas-phase calculations. The [HO─V(H$_2$O)$_4$SO$_4$] species in vacuum was modeled using a 20 × 20 × 20 Å cell with a gamma-point k-point grid. Gaussian smearing was used with a 0.01 eV smearing width for the isolated vanadium-ion complex. The metal slabs were modeled using a 6-layer 3 × 3 cell with 15 Å of vacuum spacing in the z-direction, a 5 × 5 × 1 Monkhorst Pack k-point grid,[14] and first-order Methfessel-Paxton smearing with a 0.1 eV smearing width.[15] The bottom two layers were fixed in their bulk positions, and a

dipole correction was applied in the *z*-direction. Vibrational energies of the adsorbate were calculated using finite differences with a step size of 0.015 Å, fixing all metal atoms in their bulk positions.

Results

Figure 3 below shows the free energy profiles from metadynamics of the adsorbed vanadium intermediate on all surfaces simulated.
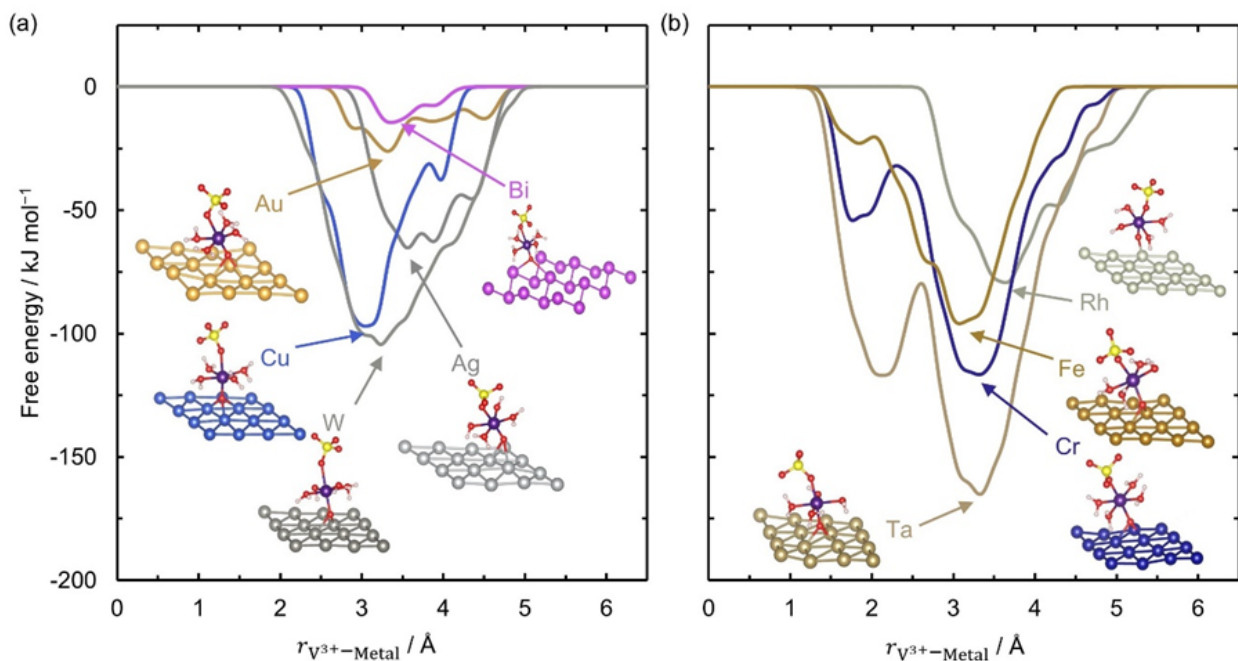

Figure 3. Computed free energy profiles of adsorbed vanadium intermediate on **(a)** Bi, Au, Ag, Cu, and W and **(b)** Rh, Fe, Cr, and Ta for V^{2+}/V^{3+} kinetics. Snapshots of the adsorbed V^{3+} complex are shown at the minimum of each free energy profile.

The adsorption energies calculated from the free energy minima are shown in **Table 1** below along with lattice parameters and adsorption energies calculated in the gas phase.

Table 1. Lattice parameters and free energies of adsorption calculated using metadynamics and static gas phase DFT calculations for all systems considered. A negative adsorption free energy indicates favorable binding while a positive adsorption energy indicates unfavorable binding.

Metal (surface facet)	Lattice parameters (Å)	Aqueous-phase adsorption energy (kJ/mol)	Gas-phase adsorption energy (kJ/mol)
Au(111)	FCC a = 4.17	−26.1	−34.3
Ag(111)	FCC a = 4.16	−64.6	5.14

Cu(111)	FCC a = 3.64	−96.5	−26.5
W(110)	BCC a = 3.175	−104.2	−257.1
Bi(111)	Rhombohedral Close Packed Distance: a = 4.63 Interlayer Distance: $\Delta z_{12} = 2.45$, $\Delta z_{23} = 1.61$	−14.5	0.00
Rh(111)	FCC a = 3.80	−79.1	−71.3
Fe(110)	BCC a = 2.84	−95.5	115.8
Cr(110)	BCC a = 2.84	−116.7	−271.9
Ta(110)	BCC a = 3.31	−165.0	−432.1

The adsorption free energies calculated in the aqueous phase using metadynamics and the gas phase using static DFT calculations are plotted against the electrode d-band center below in **Figure 4a** and **4b**, respectively, for all nine metals considered.
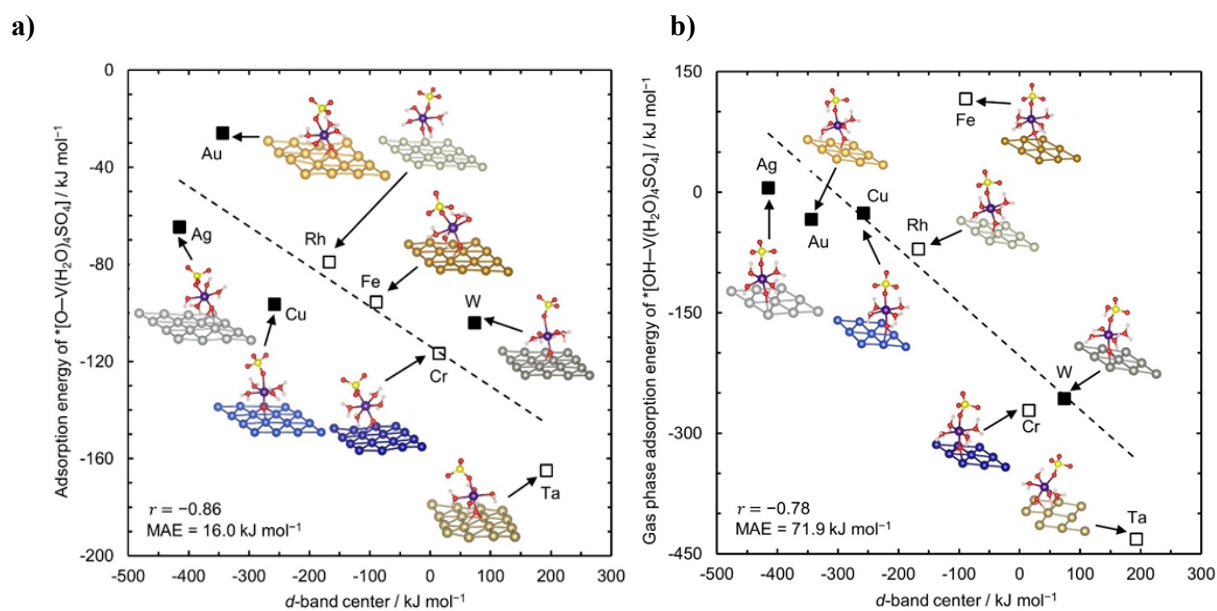
a)

b)

Figure 4. (a) Aqueous-phase and **(b)** Gas-phase adsorption free energy of vanadium intermediate vs. electrode d-band center. Images of the **(a)** geometries at the free energy minimum and **(b)** relaxed geometries of the adsorbed complexes are shown for each surface considered, with arrows pointing to the corresponding data point. Black dotted lines show linear correlations between adsorption energy and d-band center. The solid squares are the metals that are experimentally tested for kinetics and hollow squares are additional metals computationally tested to cover a larger range of d-band centers. Pearson correlation coefficient (r) and mean absolute error (MAE) for the correlations are shown.

Pearson correlation coefficients of $r = -0.86$ and -0.78 in the aqueous and gas phase, respectively, indicate that the vanadium-ion complex binds stronger to electrodes with a higher d-band center, as expected from d-band theory. A lower d-band center relative to the Fermi level leads to a greater occupancy of the antibonding orbitals and a weaker bond. The gas-phase adsorption free energy on Fe is much higher than expected based on its d-band center and does not fit the correlation. This could be due to the ferromagnetic nature of Fe. However, this effect is not observed in the aqueous phase, which more rigorously models the relevant experimental conditions of a flow battery.

Our experimental collaborators in the Singh lab used a rotating disk electrode to measure the steady-state current at different rotation rates, overpotentials, states of charge, and electrodes and used the Koutecky-Levich method to extract the contributions to the current from kinetics and mass-transfer. Current densities were normalized using the electrochemically active surface area (ECSA) and exchange current densities extracted using the Tafel method for all metals except W. For large overpotentials, the current-overpotential relationship can be approximated using the Tafel equation:

$$i = i_0 exp\left(\frac{\eta}{b}\right) \tag{5}$$

Where i is the current density, i_0 is the exchange current density (or the rate of charge transfer associated with the oxidation and reduction processes at equilibrium), η is the overpotential (or difference between the applied potential and the equilibrium redox potential), and b is the Tafel slope (an empirical fitting parameter). The Butler-Volmer method was used instead of the Tafel method for W because the current was large enough to become mass-transfer controlled (i.e. the limiting current was reached) at low overpotentials, preventing proper analysis using the Tafel method. **Figure 5** below plots the

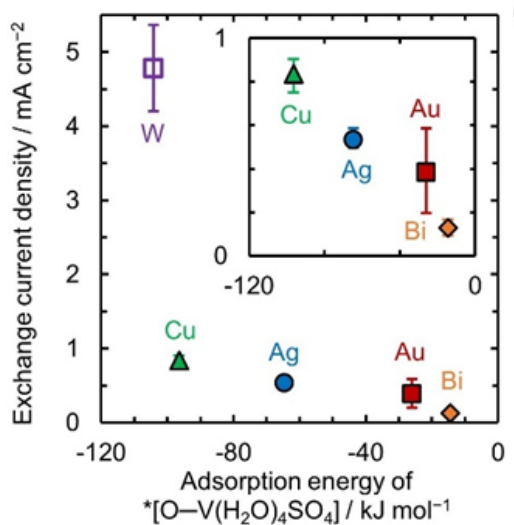exchange current densities at 50% SoC against the calculated adsorption free energy of the adsorbed intermediate.

Figure 5. Exchange current density for V^{2+}/V^{3+} CT reaction at 50% SoC in H_2SO_4 vs. calculated aqueous-phase adsorption energies of adsorbed vanadium intermediate on Au, Ag, Cu, Bi, and W electrodes. The inset shows a zoomed version of the plot excluding W.

To explore the effectiveness of the electrode d-band center as a descriptor for het-CT kinetics for other redox couples, we study how well experimentally-determined kinetic parameters from the literature correlate with d-band center. We only consider sets of data for a given redox couple measured in the same laboratory using the same method to avoid variations in experimental procedures from one laboratory to another, which can have a strong effect on the value of the apparent rate constant or exchange current density. For example, if a rotating disk electrode is not operated at a sufficiently high rotation rate, the reaction can become mass transfer controlled rather than kinetically controlled. In addition, since the electrolyte can influence the mechanism and have a strong effect on kinetics, we only compare data conducted in the same electrolyte. In addition to the results from our study for the V^{2+}/V^{3+} redox couple,[16] we also consider $Cr^{2+/3+}$ in $NaClO_4$,[17] cis-$([Co(en)_2](NCS)_2)^{0/+1}$ in $NaClO_4/HClO_4$, $[Co(NH_3)_5]NCS^{2+/1+}$ in $NaClO_4/HClO_4$,[18] $Fe^{2+/3+}$ in K_2SO_4/H_2SO_4, and $Fe^{2+/3+}$ at 0.1 M and 0.01 M in H_2SO_4.[19,20] Similarly to V^{2+}/V^{3+}, these transition metal ions adsorb to metal electrodes via a bridging anion, either present in the electrolyte or as a ligand. **Figure 6** below plots the electrode d-band center against the natural log of exchange current density (i_0), rate constant (k), or apparent rate constant (k_{app}) for these systems. It also shows that other possible descriptors, including atomic polarizability, electronegativity, and work function do not correlate as well as d-band center does for all of the redox couples considered.
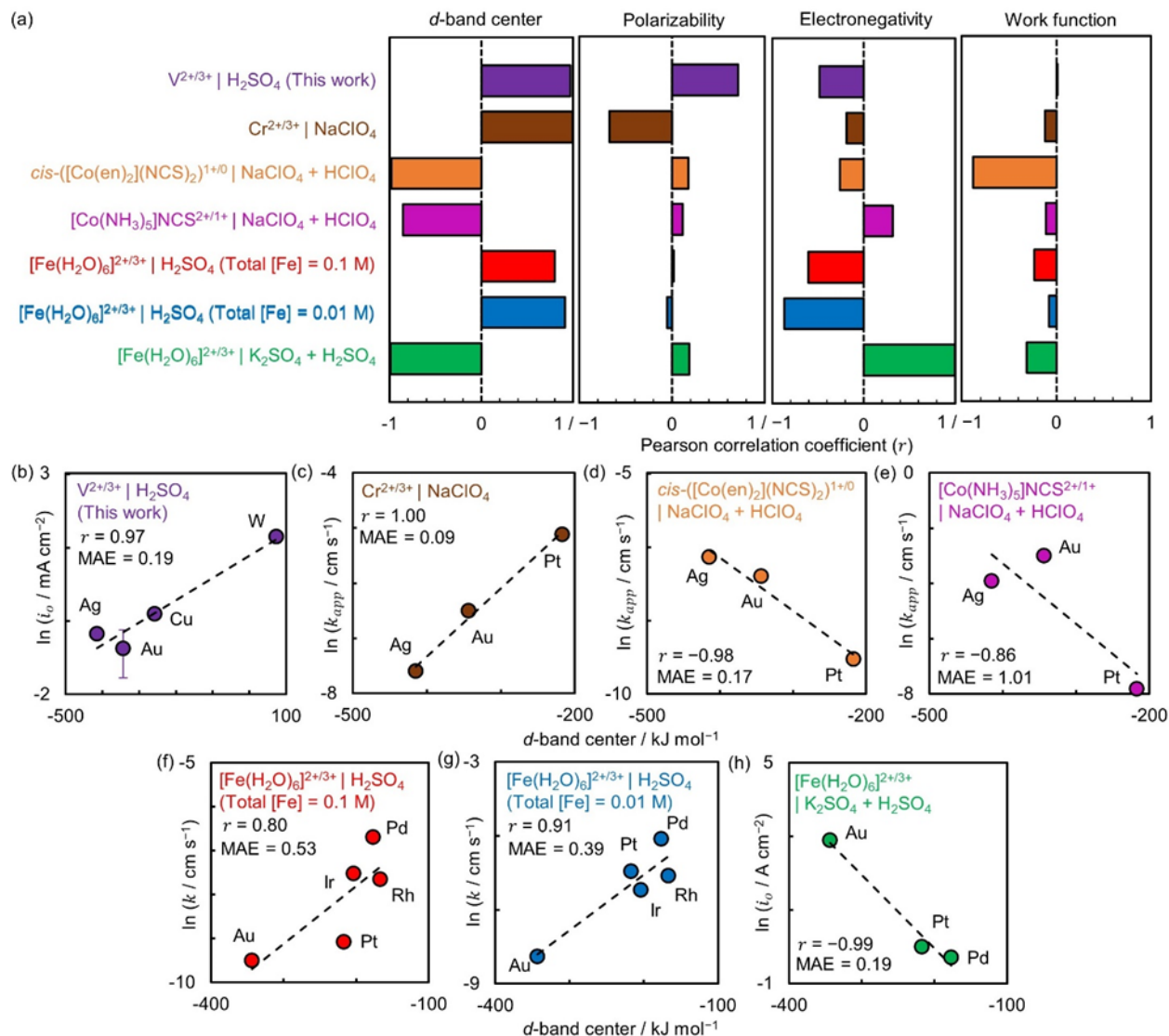
Figure 6. (a) Pearson correlation coefficient between natural logarithm of het-CT kinetics (expressed by exchange current density or rate constant) and different possible electrode descriptors for $V^{2+/3+}$ and other redox couples from the literature. **(b-h)** Plots of natural logarithm of het-CT kinetics vs. d-band center for different redox couples considered.

The strong correlations observed between rate constant or exchange current density and electrode d-band center for a variety of redox couples and electrodes indicate that the d-band center is indeed responsible for variations in redox kinetics. Depending on the redox couple and electrolyte, the correlation is either positive or negative, which can be explained by the Sabatier principle, which states that a catalyst that binds the active intermediate at the optimal strength is the most active.[5,6] Catalysts with a higher, or lower, adsorption energy result in a lower rate constant or current density. Thus, for a given system, there is an optimal d-band center for which the rate is maximized. Below this value, increasing the d-band center will increase the rate and a positive correlation is observed, while above this value increasing the d-band center will decrease the rate and a negative correlation is observed. For $[Co(NH_3)_5]NCS^{2+/1+}$ in

NaClO$_4$/HClO$_4$, it appears that Au has a close to optimal d-band center, lying at the peak of the "volcano." Further study is needed to determine the optimal d-band center for the different systems considered. The d-band center can be tuned and optimized by combining different metals via alloying or the use of core-shell nanoparticles. For the V^{2+}/V^{3+} redox couple, it appears that Ag, Au, Cu, and W lie below the optimal d-band center. Future studies could experimentally test metals with relatively high d-band centers, such as Cr or Ta, to find the optimal d-band center.

Discussion/Conclusions

Using d-band theory, the trends relating d-band center to catalytic activity can be explained in terms of a mechanistic pathway involving multiple steps upon which kinetic parameters (exchange current density i_0, apparent rate constant k_{app}, activation energy E_a, and apparent frequency factor A) depend. The free energy diagram is shown in **Figure 7a** and mechanism in **Figure 7b**.[16]
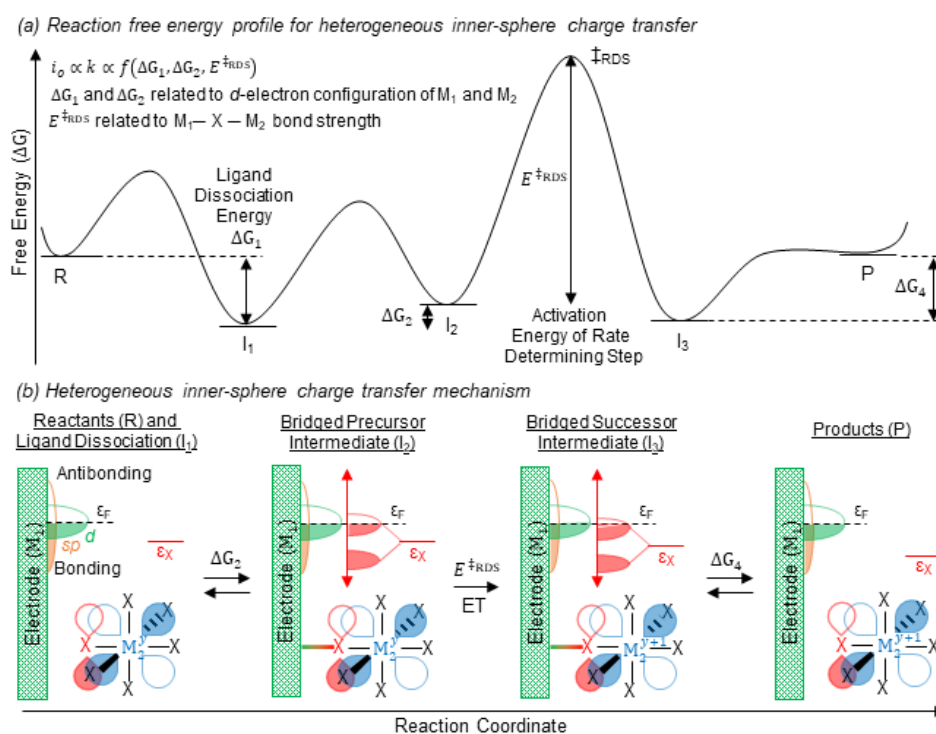

Figure 7. (a) Free energy diagram of relevant intermediates for inner-sphere transition metal-ion CT at a metal electrode including reactant R, Intermediates I$_1$, I$_2$, and I$_3$, and product P. ΔG_i is the free energy of step i and E$^{\ddagger RDS}$ is the activation barrier of the rate determining step (i.e. charge transfer). **(b)** Mechanism for heterogeneous inner-sphere CT between metals M$_1$ and M$_2$, where y is the oxidation state of metal M$_2$ and X is a neutral ligand. The density of states of metal M$_1$, d-orbitals of metal M$_2$, and p-orbital of ligand X are shown in green, blue, and red, respectively. ET denotes electron transfer, ε_X is the energy of the p-orbital of X, and ε_F is the Fermi level of the electrode.

The mechanism involves the formation of three intermediates, I$_1$, I$_2$, and I$_3$, with four elementary steps involving ligand dissociation, adsorption, electron transfer, and desorption. Based on our experimental

results, electron transfer is the rate determining step. If this is the case, the apparent frequency factor depends on the concentration of I_2, which depends on ΔG_1 and ΔG_2, and the apparent rate constant on the activation barrier E^{RDS}. Therefore, the reaction kinetics depend on ΔG_1, ΔG_2, and E^{RDS}. Based on BEP relations, E^{RDS} is related to the free energy of electron transfer, or the energy difference between I_2 and I_3. The energy of I_3 depends on the adsorption free energy of the adsorbed intermediate, ΔG_4. This energy is related to E^{RDS} by linear adsorbate scaling relations and therefore acts as a descriptor for charge transfer kinetics. **Figure 5** above shows that the exchange current density is related to ΔG_4, the adsorption free energy of the vanadium intermediate.

Trends in the reaction energetics can be explained in terms of relative occupancy of the antibonding orbital of ligand X. Greater occupancy of the antibonding orbital leads to electrostatic repulsion and thus weaker adsorption to a surface. The *d*-band model describes the position of the anti-bonding orbital of an adsorbate relative to the Fermi level, and thus its relative occupancy, based on the electrode *d*-band center. This model has previously been used to explain kinetic trends of heterogeneous reactions such as the hydrogen evolution reaction (HER) and oxygen evolution reaction (OER), which involve atomic adsorbates such as H and O.[21–23] As shown in **Figure 7b**, a higher *d*-band center relative to the Fermi level will result in a lower occupancy of the anti-bonding states of X and thus stronger adsorption. In contrast, a lower *d*-band center will result in a greater occupancy of the anti-bonding states and weaker adsorption. A stronger or weaker adsorption of X leads to a stronger or weaker adsorption energy ΔG_4 of the adsorbed intermediate, $*[X\text{-}M_2^{y+1}]$, influencing CT kinetics. Indeed, we observe a linear correlation between electrode *d*-band center and ΔG_4 (**Figure 4**), and thus the *d*-band model explains kinetic trends of het-CT reactions shown in **Figure 5** across different transition metals.

This work extends the well-known *d*-band model of heterogeneous catalysis to inner-sphere metal-ion charge transfer for the first time. This will enable the rational design of alloys or core-shell catalysts with a desired *d*-band center to maximize inner-sphere CT kinetics for energy storage applications such as redox flow batteries. Possibly, this could be used to overcome the kinetic limitations of the V^{2+}/V^{3+} CT reaction for VRFBs. This would enable increased use of intermittent renewables in the electric power grid, easing our dependence on fossil fuels and reducing greenhouse gas emissions.

References

(1) Ding, C.; Zhang, H.; Li, X.; Liu, T.; Xing, F. Vanadium Flow Battery for Energy Storage: Prospects and Challenges. *J. Phys. Chem. Lett.* **2013**, *4* (8), 1281–1294. https://doi.org/10.1021/jz4001032.
(2) Agarwal, H.; Florian, J.; Goldsmith, B. R.; Singh, N. V2+/V3+ Redox Kinetics on Glassy Carbon in Acidic Electrolytes for Vanadium Redox Flow Batteries. *ACS Energy Lett.* **2019**, *4* (10), 2368–2377. https://doi.org/10.1021/acsenergylett.9b01423.
(3) Agarwal, H.; Florian, J.; Goldsmith, B. R.; Singh, N. The Effect of Anion Bridging on Heterogeneous Charge Transfer for V2+/V3+. *Cell Reports Physical Science* **2021**, *2* (1), 100307. https://doi.org/10.1016/j.xcrp.2020.100307.
(4) Florian, J.; Agarwal, H.; Singh, N.; R. Goldsmith, B. Why Halides Enhance Heterogeneous Metal Ion Charge Transfer Reactions. *Chemical Science* **2021**, *12* (38), 12704–12710. https://doi.org/10.1039/D1SC03642D.
(5) Energy Trends in Catalysis. In *Fundamental Concepts in Heterogeneous Catalysis*; John Wiley & Sons, Ltd, 2014; pp 85–96. https://doi.org/10.1002/9781118892114.ch6.
(6) Activity and Selectivity Maps. In *Fundamental Concepts in Heterogeneous Catalysis*; John Wiley &

Sons, Ltd, 2014; pp 97–113. https://doi.org/10.1002/9781118892114.ch7.

(7) Nørskov, J. K.; Studt, F.; Abild-Pedersen, F.; Bligaard, T.; Nørskov, J. K. *Fundamental Concepts in Heterogeneous Catalysis*; John Wiley & Sons, Incorporated: Somerset, UNITED STATES, 2014.

(8) Laio, A.; Parrinello, M. Escaping Free-Energy Minima. *Proceedings of the National Academy of Sciences* **2002**, *99* (20), 12562–12566. https://doi.org/10.1073/pnas.202427399.

(9) Iannuzzi, M.; Laio, A.; Parrinello, M. Efficient Exploration of Reactive Potential Energy Surfaces Using Car-Parrinello Molecular Dynamics. *Phys. Rev. Lett.* **2003**, *90* (23), 238302. https://doi.org/10.1103/PhysRevLett.90.238302.

(10) Kresse, G.; Joubert, D. From Ultrasoft Pseudopotentials to the Projector Augmented-Wave Method. *Phys. Rev. B* **1999**, *59* (3), 1758–1775. https://doi.org/10.1103/PhysRevB.59.1758.

(11) Perdew, J. P.; Burke, K.; Ernzerhof, M. Generalized Gradient Approximation Made Simple. *Phys Rev Lett* **1996**, *77* (18), 3865–3868. https://doi.org/10.1103/PhysRevLett.77.3865.

(12) Nosé, S. A Unified Formulation of the Constant Temperature Molecular Dynamics Methods. *J. Chem. Phys.* **1984**, *81* (1), 511–519. https://doi.org/10.1063/1.447334.

(13) Larsen, A. H.; Mortensen, J. J.; Blomqvist, J.; Castelli, I. E.; Christensen, R.; Dułak, M.; Friis, J.; Groves, M. N.; Hammer, B.; Hargus, C.; Hermes, E. D.; Jennings, P. C.; Jensen, P. B.; Kermode, J.; Kitchin, J. R.; Kolsbjerg, E. L.; Kubal, J.; Kaasbjerg, K.; Lysgaard, S.; Maronsson, J. B.; Maxson, T.; Olsen, T.; Pastewka, L.; Peterson, A.; Rostgaard, C.; Schiøtz, J.; Schütt, O.; Strange, M.; Thygesen, K. S.; Vegge, T.; Vilhelmsen, L.; Walter, M.; Zeng, Z.; Jacobsen, K. W. The Atomic Simulation Environment—a Python Library for Working with Atoms. *J. Phys.: Condens. Matter* **2017**, *29* (27), 273002. https://doi.org/10.1088/1361-648X/aa680e.

(14) Monkhorst, H. J.; Pack, J. D. Special Points for Brillouin-Zone Integrations. *Phys. Rev. B* **1976**, *13* (12), 5188–5192. https://doi.org/10.1103/PhysRevB.13.5188.

(15) Methfessel, M.; Paxton, A. T. High-Precision Sampling for Brillouin-Zone Integration in Metals. *Phys. Rev. B* **1989**, *40* (6), 3616–3621. https://doi.org/10.1103/PhysRevB.40.3616.

(16) Agarwal, H.; Florian, J.; Pert, D.; Goldsmith, B. R.; Singh, N. Explaining Kinetic Trends of Inner-Sphere Transition-Metal-Ion Redox Reactions on Metal Electrodes. *ACS Catal.* **2023**, 2223–2233. https://doi.org/10.1021/acscatal.2c05694.

(17) Barr, S. W.; Guyer, K. L.; Weaver, M. J. The Dependence of the Kinetics of Some Simple Outer-Sphere Electrode Reactions on the Nature of the Electrode Material. *Journal of Electroanalytical Chemistry and Interfacial Electrochemistry* **1980**, *111* (1), 41–59. https://doi.org/10.1016/S0022-0728(80)80074-X.

(18) Barr, S. W.; Weaver, M. J. Intramolecular Electron Transfer at Metal Surfaces. 1. Relative Energetics of Some Corresponding Outer- and Inner-Sphere Pathways Involving Halide and Pseudohalide Bridging Ligands. *Inorg. Chem.* **1984**, *23* (12), 1657–1663. https://doi.org/10.1021/ic00180a007.

(19) Bockris, J. O.; Mannan, R. J.; Damjanovic, A. Dependence of the Rate of Electrodic Redox Reactions on the Substrate. *J. Chem. Phys.* **1968**, *48* (5), 1898–1904. https://doi.org/10.1063/1.1668987.

(20) Bochmann, H. G.; Vielstich, W. On the Reaction Rate of the Fe^{2+}/Fe^{3+} Redox Couple in Sulfate Solution. *Electrochimica Acta* **1988**, *33* (6), 805–809. https://doi.org/10.1016/S0013-4686(98)80011-X.

(21) Lima, F. H. B.; Zhang, J.; Shao, M. H.; Sasaki, K.; Vukmirovic, M. B.; Ticianelli, E. A.; Adzic, R. R. Catalytic Activity−d-Band Center Correlation for the O2 Reduction Reaction on Platinum in Alkaline Solutions. *J. Phys. Chem. C* **2007**, *111* (1), 404–410. https://doi.org/10.1021/jp065181r.

(22) Greeley, J.; Nørskov, J. K.; Kibler, L. A.; El-Aziz, A. M.; Kolb, D. M. Hydrogen Evolution Over Bimetallic Systems: Understanding the Trends. *ChemPhysChem* **2006**, *7* (5), 1032–1035. https://doi.org/10.1002/cphc.200500663.

(23) Leonard, K. C.; Bard, A. J. Pattern Recognition Correlating Materials Properties of the Elements to Their Kinetics for the Hydrogen Evolution Reaction. *J. Am. Chem. Soc.* **2013**, *135* (42), 15885–15889. https://doi.org/10.1021/ja407394q.